

Experimental demonstration of entanglement-enabled universal quantum cloning in a circuit

Zhen-Biao Yang¹, Pei-Rong Han¹, Xin-Jie Huang¹, Wen Ning¹, Hekang Li², Kai Xu^{2,3,*}, Dongning Zheng^{2,3}, Heng Fan^{2,3,†} and Shi-Biao Zheng^{1‡}

*1.Fujian Key Laboratory of Quantum Information and Quantum Optics,
College of Physics and Information Engineering,
Fuzhou University, Fuzhou, Fujian 350108, China*

*2.Institute of Physics and Beijing National Laboratory for Condensed Matter Physics,
Chinese Academy of Sciences, Beijing 100190, China and*

*3.CAS Center for Excellence in Topological Quantum Computation,
University of Chinese Academy of Sciences, Beijing 100190, China*

No-cloning theorem forbids perfect cloning of an unknown quantum state. A universal quantum cloning machine (UQCM), capable of producing two copies of any input qubit with the optimal fidelity, is of fundamental interest and has applications in quantum information processing. This is enabled by delicately tailored nonclassical correlations between the input qubit and the copying qubits, which distinguish the UQCM from a classical counterpart, but whose experimental demonstrations are still lacking. We here implement the UQCM in a superconducting circuit, and investigate these correlations. The measured entanglements well agree with our theoretical prediction that they are independent of the input state, and thus constitute a universal quantum behavior of the UQCM that was not previously revealed. Another feature of our experiment is realization of deterministic and individual cloning, in contrast to previously demonstrated UQCMs, which either were probabilistic or did not constitute true cloning of individual qubits.

I. INTRODUCTION

An unknown quantum state cannot be cloned perfectly due to the linearity associated with the unitary transformation of quantum mechanics. This feature, discovered by Wootters and Zurek in 1982 and known as the no-cloning theorem [1], represents one of the fundamental differences between quantum information and classical information. In particular, it ensures the security of quantum cryptography schemes [2–4].

Because of the impossibility of perfect quantum cloning, much attention has been paid to the possibility of producing copies close to the original states. In the seminal paper by Buzek and Hillery, a universal quantum cloning machine (UQCM) was proposed, which produces two identical approximate copies via controllably entangling them with the original qubit [5]. The output state of each of these two copy qubits has a fidelity of 5/6 to the input state, which is independent of the input state and was proven to be optimal [6, 7]. Besides fundamental interest, quantum cloning can be used to improve the performance of some quantum computational tasks [8], to distribute quantum information, and to realize minimal disturbance measurements [9]. The UQCM has been

*Electronic address: kaixu@iphy.ac.cn

†Electronic address: hfan@iphy.ac.cn

‡Electronic address: t96034@fzu.edu.cn

reported in nuclear magnetic resonance systems [10, 11], but where the true cloning of individual quantum systems cannot be achieved due to the ensemble aspect. Huang et al. presented a proof-of-principle demonstration in an optical system [12], where only a single photon was involved; its polarization state was copied onto one path freedom degree.

Several optical experiments have been reported, where the state of a photon was copied onto another photon [13–17], but the cloning processes are probabilistic for lack of a deterministic two-qubit controlled gate between different photons in these experiments.

Besides the limitation of ensemble aspect or probabilistic nature, previous experiments did not reveal the non-classical correlations between the original input qubit and the copying qubits. These correlations enable the information carried by the input state to be equally imprinted on the clones with the optimal fidelity, and represent the most fundamental difference between the UQCM and a classical cloning machine. Quantitative characterization of these correlations is important for revealing the genuine quantum behavior of the UQCM, which is closely related to the universality and optimality of the copying operation.

We here adapt a scheme proposed in the context of cavity quantum electrodynamics [18] to a superconducting circuit involving Xmon qubits controllably coupled to a bus resonator. The high degree of control over the qubit-qubit interactions enables realizations of all gate operations required for approximately cloning the state of each qubit in a deterministic way. We indicate the universality of the implemented UQCM, and quantitatively characterize the entanglement between the input qubit and each of the copy qubits. The results confirm our theoretical prediction that this entanglement is also input-state-independent, and represents a universal quantum

feature of the UQCM. The entanglement between the two copy qubits is also measured.

II. RESULTS

A. Implementation of UQCM.

The sample used to perform the experiment involves five Xmon qubits [19], three of which are employed in our experiment and labeled from Q_1 to Q_3 ; these qubits are almost symmetrically coupled to a central bus resonator, as sketched in Fig. 1a. The resonator has a fixed frequency of $\omega_r/2\pi = 5.588$ GHz, while the frequencies of the qubits are individually adjustable, which enables us to tailor the system dynamics to accomplish the copying task. The Hamiltonian for the total system is

$$H = \hbar \left[\omega_r a^\dagger a + \sum_{j=1}^3 \omega_{q,j} |1_j\rangle \langle 1_j| + \sum_{j=1}^3 g_j (a^\dagger S_j^- + a S_j^+) \right], \quad (1)$$

where a^\dagger and a are the photonic creation and annihilation operators for the resonator, respectively, $S_j^+ = |1_j\rangle \langle 0_j|$ and $S_j^- = |0_j\rangle \langle 1_j|$ are the flip operators for Q_j , with $|0_j\rangle$ and $|1_j\rangle$ being its ground and first excited states separated by an energy gap $\hbar\omega_{q,j}$, g_j are the corresponding qubit-resonator coupling strengths, and \hbar is the reduced Planck constant. In our sample these coupling strengths are almost identical, e.g., $g_j \simeq g \simeq 2\pi \times 20$ MHz. The system parameters are detailed in Supplementary Note 3. The qubit frequency tunability makes the system dynamics programable.

When two or more qubits are detuned from the resonator by the same amount much larger than g , they are coupled by virtual photon exchange [20–30]. In our experiment, Q_1 acts as the original qubit whose state is to be cloned, and Q_2 and Q_3 are used as the copying qubits.

The experimental sequence for realizing the UQCM

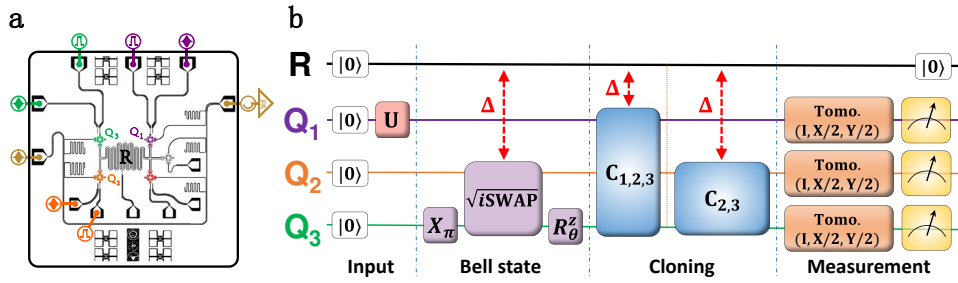


FIG. 1: Device image and experimental scheme for the implementation of UQCM. **a** The device image. The device sample has five superconducting Xmon Qubits (three of them are used and are labeled from Q_1 to Q_3) and a central bus resonator R ; the qubits' manipulation and their coupling to the resonator and the measurement are controlled by microwave pulses injected onto the circuit sample. **b** Before the copying operation, all qubits are initialized to their ground state at the corresponding idle frequencies. The whole procedure can be divided into four steps: Preparation of the input state through a unitary rotation at the idle frequency, denoted as U ; entanglement of Q_2 and Q_3 with Bell type, achieved by a π rotation X_π on Q_3 , the Q_2 - Q_3 \sqrt{i} SWAP gate, and a small Z pulse on Q_3 realizing a rotation R_θ^z for phase compensation; cloning of the input state onto Q_2 and Q_3 , realized by resonator-induced couplings $C_{1,2,3}$ and $C_{2,3}$; output state tomography. $C_{1,2,3}$ is implemented by tuning Q_2 and Q_3 on resonance with Q_1 at the working frequency, while $C_{2,3}$ realized by tuning Q_1 back to its idle frequency, leaving Q_2 and Q_3 coupled to each other. Note that in our experiment, steps 1 and 2 are completed simultaneously for the sake of reducing qubits' decoherence, see Supplementary Note 4 for the details.

with our setup is shown in Fig. 1b. The experiment starts with initializing the resonator to the vacuum state $|0_r\rangle$ and the qubits to their ground state $|0_10_20_3\rangle$ at their idle frequencies. These idle frequencies are highly detuned from the resonator frequency and off-resonant with each other, ensuring each qubit to be effectively decoupled from the resonator and other qubits when staying at its idle frequency. After the initialization, a suitable rotation is applied to Q_1 to prepare it in the state to be cloned

$$|\psi_{\text{in}}\rangle = \alpha |0_1\rangle + \beta |1_1\rangle, \quad (2)$$

where α and β are complex numbers, satisfying $|\alpha|^2 + |\beta|^2 = 1$. Prior to the copying operation, we have to prepare Q_2 and Q_3 in the entangled state $|\psi_{2,3}^+\rangle = (|1_20_3\rangle + |0_21_3\rangle)/\sqrt{2}$. To prepare this state, we first transform Q_3 to the excited state $|1_3\rangle$ by a π rotation X_π , and then tune Q_2 and Q_3 to the working frequency $\omega_w/2\pi = 5.44$ GHz. With this setting, the resonator will not exchange

photons with the qubits and remain in the ground state due to the large detuning, but can mediate energy swapping between the two qubits [20]. After a duration of 57.7 ns, a \sqrt{i} SWAP gate is realized, which evolves these two qubits to the state $(e^{i\theta} |1_20_3\rangle + |0_21_3\rangle)/\sqrt{2}$, where $\theta = \pi/2 + \theta_d$, with θ_d being the extra dynamical phase accumulated during the frequency tuning process. To cancel the phase θ , Q_3 is tuned to the frequency 5.311 GHz, where the rotation $R_\theta^z = e^{i\theta|1_3\rangle\langle 1_3|}$ is realized after a duration of 30 ns.

After the production of $|\psi_{2,3}^+\rangle$, Q_2 and Q_3 are tuned on resonance with Q_1 at the working frequency, where these qubits are red-detuned from the resonator by the same amount $\Delta = 2\pi \times 148$ MHz. With this setting, the resonator does not exchange photons with the qubits due to the large detuning, but can mediate a coupling of strength $\lambda = g^2/\Delta$ between any two of these qubits. The resonator will remain in the ground state during this

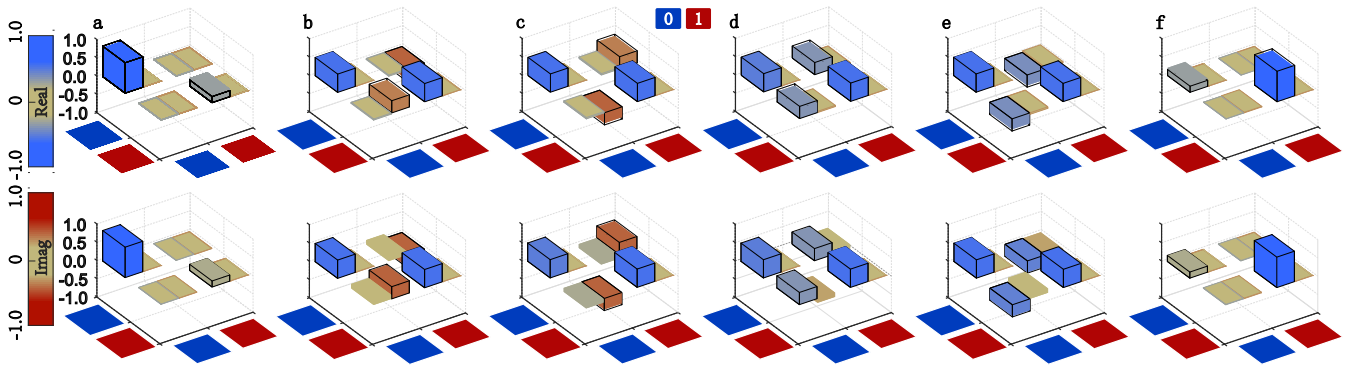


FIG. 2: Reconstructed output states of Q_2 and Q_3 for six input states: **a** $|01\rangle$; **b** $(|01\rangle + i|11\rangle)/\sqrt{2}$; **c** $(|01\rangle - i|11\rangle)/\sqrt{2}$; **d** $(|01\rangle + |11\rangle)/\sqrt{2}$; **e** $(|01\rangle - |11\rangle)/\sqrt{2}$; **f** $|11\rangle$. The measured output density matrices of Q_2 and Q_3 are respectively displayed in the upper and lower panels. Each matrix element is characterized by two color bars, one for the real part and the other for the imaginary part. The black wire frames denote the corresponding matrix elements of the output states yielded by the perfect UQCM.

process, and can be discarded in the description of the system dynamics. In the interaction picture, the state evolution of the qubits is governed by the effective Hamiltonian [20, 21]

$$H_e = -\lambda \sum_{j,k=1}^3 S_j^+ S_k^-, \quad j \neq k. \quad (3)$$

Under this Hamiltonian, Q_2 and Q_3 symmetrically interact with Q_1 through excitation exchange, with the number of the total excitations being conserved. After an interaction time $\tau = 2\pi/9\lambda$, the three-qubit coupling $C_{1,2,3}$ evolves Q_1 , Q_2 and Q_3 to the entangled state

$$\alpha \left[\sqrt{\frac{2}{3}} |11\rangle |02\rangle |03\rangle + \sqrt{\frac{1}{3}} e^{-i\pi/3} |01\rangle |\psi_{2,3}^+\rangle \right] + \beta \left[\sqrt{\frac{2}{3}} |01\rangle |12\rangle |13\rangle + \sqrt{\frac{1}{3}} e^{-i\pi/3} |11\rangle |\psi_{2,3}^+\rangle \right]. \quad (4)$$

Then Q_1 is tuned back to its idle frequency of 5.367 GHz and decoupled from Q_2 and Q_3 , which remain at the working frequency and continue to interact with each other. The state components $|02\rangle |03\rangle$ and $|12\rangle |13\rangle$ are eigenstates of the two-qubit interaction Hamiltonian $H'_e = -\lambda (S_2^+ S_3^- + S_2^- S_3^+)$ with the zero eigenvalue, while $|\psi_{2,3}^+\rangle$ is an eigenstate of H'_e with the eigenvalue

of $-\lambda$. As a result, this swapping interaction does not affect $|02\rangle |03\rangle$ and $|12\rangle |13\rangle$, but produces a phase shift $\lambda\tau'$ to $|\psi_{2,3}^+\rangle$, with τ' being the interaction time. With the choice $\tau' = \pi/3\lambda$, the two-qubit coupling $C_{2,3}$ cancels the phase factor $e^{-i\pi/3}$ associated with $|\psi_{2,3}^+\rangle$, evolving the three qubits to [18]

$$\alpha \left[\sqrt{\frac{2}{3}} e^{i\phi} |11\rangle |02\rangle |03\rangle + \sqrt{\frac{1}{3}} |01\rangle |\psi_{2,3}^+\rangle \right] + \beta \left[\sqrt{\frac{2}{3}} |01\rangle |12\rangle |13\rangle + \sqrt{\frac{1}{3}} e^{i\phi} |11\rangle |\psi_{2,3}^+\rangle \right], \quad (5)$$

where the phase ϕ is due to the frequency shift of Q_1 during the Q_2 - Q_3 interaction, which does not affect the reduced density matrices for both Q_2 and Q_3 , each of which in the basis $\{|0\rangle, |1\rangle\}$ is given by

$$\begin{pmatrix} \frac{5}{6} |\alpha|^2 + \frac{1}{6} |\beta|^2 & \frac{2}{3} \alpha \beta^* \\ \frac{2}{3} \alpha^* \beta & \frac{1}{6} |\alpha|^2 + \frac{5}{6} |\beta|^2 \end{pmatrix}. \quad (6)$$

For the perfect UQCM, the fidelity of these two output copiers with respect to the input state $|\psi_{in}\rangle$ is 5/6, irrespective of the probability amplitudes α and β associated with the components $|0\rangle$ and $|1\rangle$. Due to the nonuniform qubit-resonator couplings and the existence of the direct but also nonuniform qubit-qubit couplings in our

device [26–30], each qubit is asymmetrically coupled to the other two qubits with the effective coupling strengths slightly different from λ . In order to produce the optimal outcome, the coupling operations C_{123} and C_{23} are calibrated simultaneously, and consequently, the optimal coupling times τ and τ' that deviate from the values for the ideal case are 40.8 ns and 69.5 ns, respectively. After the copy process, Q_2 and Q_3 are tuned back to their idle frequencies of 5.223 GHz and 5.311 GHz, respectively.

B. Characterization of performance.

We characterize the performance of the UQCM by preparing different input states $\{|0_1\rangle, (|0_1\rangle + i|1_1\rangle)/\sqrt{2}, (|0_1\rangle - i|1_1\rangle)/\sqrt{2}, (|0_1\rangle + |1_1\rangle)/\sqrt{2}, (|0_1\rangle - |1_1\rangle)/\sqrt{2}, |1_1\rangle\}$, and measuring the corresponding output states of Q_2 and Q_3 through quantum state tomography (See Supplementary Note 7). Note that, for the tomography in our experiment, the readout calibration is performed to correct the measured probabilities for the qubit states according to the qubits' $|0\rangle$ - and $|1\rangle$ -state measurement fidelities (see Supplementary Table 1 and Note 6). The measured density matrices for the clones of the above-mentioned six input states are respectively displayed in Fig. 2a-f, where the upper and lower panels denote the measured output density matrices of Q_2 and Q_3 , respectively. The fidelities of the output states of Q_2 (Q_3) to these six ideal input states, defined as $F = \langle \psi_{\text{in}} | \rho_{\text{out}} | \psi_{\text{in}} \rangle$, are respectively 0.784 ± 0.002 (0.824 ± 0.002), 0.786 ± 0.001 (0.818 ± 0.003), 0.784 ± 0.002 (0.832 ± 0.002), 0.788 ± 0.002 (0.831 ± 0.001), 0.786 ± 0.002 (0.832 ± 0.001), and 0.785 ± 0.002 (0.832 ± 0.001), where ρ_{out} denotes the measured density matrix for the corresponding output clone. Each of these fidelities is close to the optimal value $5/6$, confirming the performance of the UQCM is independent of the input state. The slight difference between the output states of the two

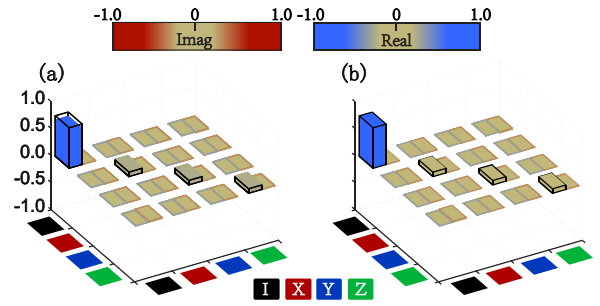


FIG. 3: Process tomography. **a** Measured process matrix associated with the output state of Q_2 . **b** Measured process matrix associated with Q_3 's output state. The black wire frames denote the corresponding process matrix elements of the perfect UQCM.

copy qubits is mainly due to direct qubit-qubit couplings. These nonuniform couplings also make the qualities of the output states slightly depend on the input state. We note that for each of the six input states, the output state of Q_3 has a fidelity very close to the theoretical upper bound. This is partly due to the asymmetry between the two clones. The other reason is that the qubit-qubit couplings during the copy process partly protect the qubits from dephasing, so that the real T_2 times of the qubits coupled at the working frequency are longer than the corresponding results listed in Supplementary Table 1, which are measured without qubit-qubit couplings [27, 28].

To further examine the performance of the UQCM, we perform the quantum process tomography (See Supplementary Note 7), achieved by preparing the above mentioned six distinct input states, and measuring them and the corresponding output states of Q_2 and Q_3 through quantum state tomography. The measured process matrices associated with the output states of Q_2 and Q_3 , $\chi_{\text{meas},2}$ and $\chi_{\text{meas},3}$, are respectively presented in Fig. 3a and 3b, respectively. The fidelities of $\chi_{\text{meas},2}$ and $\chi_{\text{meas},3}$ with respect to the ideal cloning process χ_{id} , defined as $F = \text{Tr}(\chi_{\text{meas}}\chi_{\text{id}})$, are 0.679 ± 0.001 and 0.743 ± 0.002 ,

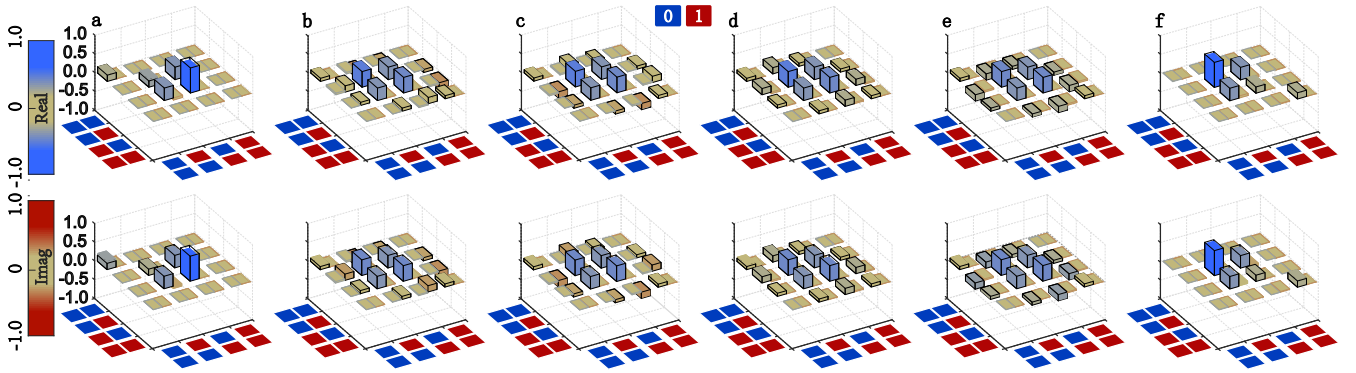


FIG. 4: Measured Q_1 - Q_2 and Q_1 - Q_3 output density matrices for input states: **a** $|0_1\rangle$; **b** $(|0_1\rangle + i|1_1\rangle)/\sqrt{2}$; **c** $(|0_1\rangle - i|1_1\rangle)/\sqrt{2}$; **d** $(|0_1\rangle + |1_1\rangle)/\sqrt{2}$; **e** $(|0_1\rangle - |1_1\rangle)/\sqrt{2}$; **f** $|1_1\rangle$. For clarity, a single-qubit z-axis rotation is numerically applied to cancel the phase of the extra phase accumulated due to the qubits' frequency shift. The measured Q_1 - Q_2 and Q_1 - Q_3 output density matrices are displayed in the upper and lower panels, respectively. The black wire frames denote the corresponding density matrices produced by the perfect UQCM.

respectively. These process fidelities are close to the result of the perfect UQCM, 0.75, demonstrating a good quantum control over the multiqubit-resonator system.

C. Demonstration of universal entanglement behavior

The nonclassical correlations between the original input qubit and the clones play an essential role in implementation of the UQCM and represents one of the most fundamental differences between universal quantum and classical cloning, but have not been quantitatively investigated. Characterization of these correlations is important for understanding the quantum behavior of the UQCM. We find that the degree of the entanglement between each output clone and the original input qubit, quantified by concurrence [31], is $2/3$ for an ideal UQCM, which is independent of the input state (see Supplementary Note 1). To detect these nonclassical correlations, we respectively measure the joint Q_1 - Q_2 and Q_1 - Q_3 output density matrices. The results for the six input states $\{|0_1\rangle, (|0_1\rangle + i|1_1\rangle)/\sqrt{2}, (|0_1\rangle - i|1_1\rangle)/\sqrt{2}, (|0_1\rangle + |1_1\rangle)/\sqrt{2}, (|0_1\rangle - |1_1\rangle)/\sqrt{2}, |1_1\rangle\}$ are displayed in

Fig. 4a-f, where the upper and lower panels correspond to the joint Q_1 - Q_2 and Q_1 - Q_3 output density matrices, respectively. For clarity of display, a single-qubit z-axis rotation is numerically applied to cancel the extra phase produced by the qubits' frequency shift, which does not affect the entanglement. The output Q_1 - Q_2 concurrences associated with these six input states are 0.667 ± 0.008 , 0.557 ± 0.005 , 0.554 ± 0.006 , 0.556 ± 0.007 , 0.569 ± 0.007 , and 0.590 ± 0.008 , while the corresponding output Q_1 - Q_3 concurrences are 0.565 ± 0.011 , 0.453 ± 0.008 , 0.457 ± 0.005 , 0.468 ± 0.005 , 0.459 ± 0.007 , and 0.511 ± 0.006 , respectively. As a nonzero concurrence indicates the existence of entanglement, these results unambiguously demonstrate that each of the two copy qubits is highly entangled with the original qubit, and the two copy qubits are also entangled. When the original qubit is traced out, the concurrence between the two copy qubits is $1/3$ for an ideal UQCM (see Supplementary Note 1), which is also input-state independent [32]. To verify this entanglement, we perform the joint Q_2 - Q_3 output state tomography. The reconstructed joint Q_2 - Q_3 density matrices for the six input states are displayed in Supplemen-

tary Note 5. The Q_2 - Q_3 concurrences associated with these six measured density matrices are 0.236 ± 0.012 , 0.076 ± 0.007 , 0.076 ± 0.006 , 0.079 ± 0.007 , 0.088 ± 0.005 , and 0.180 ± 0.010 , respectively. These results indicate that for the input superposition state the output Q_2 - Q_3 entanglement is much more affected by the decoherence effect compared to the case with input $|0_1\rangle$ - or $|1_1\rangle$ -state. This can be interpreted as follows. Since the direct couplings between the qubits are asymmetric, after the copy process, different state components of the final three-qubit state will accumulate different phases. For each input superposition state, the $Q_2 - Q_3$ concurrence on these phases is a cosine function of these phases, which is very different from the modulation of the fidelity of the output state of each copy qubit (see Supplementary Note 2). With the present system parameters, the value of the modulation function of the $Q_2 - Q_3$ concurrence is much smaller than that of the fidelity of the output state of each copy qubit, which approximates to the maximum. Consequently, the output $Q_2 - Q_3$ entanglement for the input superposition state is much smaller than that for the input $|0\rangle$ - or $|1\rangle$ -state; while the output state fidelity of each qubit is almost input-state-independent. The existence of concurrence between any two of the three qubits confirm they are in a genuine three-particle entangled state, revealing the fundamental difference between a quantum cloning process and a classical one.

III. DISCUSSION

We have demonstrated universal cloning of an arbitrary state of an individual qubit with a circuit QED setup, where all the quantum operations necessary for constructing a UQCM network are deterministically realized. We characterize the performance of the UQCM by quantum state tomography, confirming the universality of the copying process. We measure the entangle-

ment between each copy qubit and the original qubit, with the results being in well agreement with the theoretical prediction that this entanglement is input-state-independent and represents a universal quantum behavior of the UQCM. We further measure the entanglement between the two clones, verifying the existence of true three-particle entanglement at the output. These results underline the fact that the universal entanglement behavior underlies the performance of the UQCM.

IV. DATA AVAILABILITY

All data needed to evaluate the conclusions in the paper are present in the paper and/or the Supplementary Materials. Additional data related to this paper may be requested from the authors.

V. CODE AVAILABILITY

All codes used in the paper are available from the corresponding authors upon reasonable request.

VI. ACKNOWLEDGMENTS

We thank Haohua Wang at Zhejiang University for technical support. This work was supported by the National Natural Science Foundation of China (Grant No. 11674060, No. 11874114, No. 11875108, No. 11934018, No. 11904393 and No. 92065114), the Strategic Priority Research Program of Chinese Academy of Sciences (Grant No. XDB28000000), and the Natural Science Foundation of Fujian Province under Grant No. 2018J01412.

VII. AUTHOR CONTRIBUTIONS

S.-B.Z. conceived the experiment. Z.-B.Y., P.-R.H., X.-J.H., and K.X. performed the experiment and analyzed the data with the assistance of W. N. H.L. and D.Z. provided the devices used for the experiment. S.-B.Z., Z.-B.Y., K.X. and H.F. wrote the manuscript with

feedbacks from all authors.

VIII. COMPETING INTERESTS

The authors declare that they have no competing interests.

-
- [1] Wootters, W. K. & Zurek, W. H. A single quantum cannot be cloned. *Nature* (London) **299**, 802-803 (1982).
- [2] Gisin, N., Ribordy, G., Tittel, W. & Zbinden, H. Quantum cryptography. *Rev. Mod. Phys.* **74**, 145-195 (2002).
- [3] Scarani, V., Iblisdir, S., Gisin, N. & Acín, A. Quantum Cloning. *Rev. Mod. Phys.* **77**, 1225-1256 (2005).
- [4] Fan, H. et al. Quantum cloning machines and the applications. *Phys. Rep.* **544**, 241-322 (2014).
- [5] Bužek, V. & Hillery, M. Quantum copying: Beyond the no-cloning theorem. *Phys. Rev. A* **54**, 1844-1852 (1996).
- [6] Gisin, N., & Massar, S. Optimal quantum cloning machines. *Phys. Rev. Lett.* **79**, 2153-2156 (1997).
- [7] Bruß, D. et al. Optimal universal and state-dependent quantum cloning. *Phys. Rev. A* **57**, 2368-2378 (1998).
- [8] Galvão, E. F. & Hardy, L. Cloning and quantum computation. *Phys. Rev. A* **62**, 022301 (2000).
- [9] Ricci, M. et al. Separating the classical and quantum information via quantum cloning. *Phys. Rev. Lett.* **95**, 090504 (2005).
- [10] Cummins, H. K. et al. Approximate quantum cloning with nuclear magnetic resonance. *Phys. Rev. Lett.* **88**, 187901 (2002).
- [11] Du, J. et al. Experimental quantum cloning with prior partial information. *Phys. Rev. Lett.* **94**, 040505 (2005).
- [12] Huang, Y. H. et al. Optical realization of universal quantum cloning. *Phys. Rev. A* **64**, 012315 (2001).
- [13] Linares, A. L., Simon, C., Howell, J. C. & Bouwmeester, D. Experimental quantum cloning of single photons. *Science* **296**, 712-714 (2002).
- [14] Fasel, S., Gisin, N., Ribordy, G., Scarani, V. & Zbinden, H. Quantum cloning with an optical fiber amplifier. *Phys. Rev. Lett.* **89**, 107901 (2002).
- [15] Ricci, M., Sciarrino, F., Sias, C., & Martini, F. de. Teleportation scheme implementing the universal optimal quantum cloning machine and the universal NOT gate. *Phys. Rev. Lett.* **92**, 047901 (2004).
- [16] Irvine, W. T. M., Lamas-Linares, A., Dood, M. J. A. de. & Bouwmeester, D. Optimal quantum cloning on a beam splitter. *Phys. Rev. Lett.* **92**, 047902 (2004).
- [17] Nagali, E. et al. Optimal quantum cloning of orbital angular momentum photon qubits through Hong-Ou-Mandel coalescence. *Nat. Photon.* **3**, 720-723 (2009).
- [18] Zou, X., Pahlke, K., & Mathis, W. Scheme for the implementation of a universal quantum cloning machine via cavity-assisted atomic collisions in cavity QED. *Phys. Rev. A* **67**, 024304 (2003).
- [19] Song, C. et al. Continuous-variable geometric phase and its manipulation for quantum computation in a superconducting circuit. *Nat. Commun.* **8**, 1061 (2017).
- [20] Zheng, S. B. & Guo, G. C. Efficient Scheme for Two-Atom Entanglement and Quantum Information Processing in Cavity QED. *Phys. Rev. Lett.* **85**, 2392-2395 (2000).
- [21] Zheng, S. B. One-Step Synthesis of Multiatom Greenberger-Horne-Zeilinger States. *Phys. Rev. Lett.* **87**, 230404 (2001).
- [22] Zheng, S. B., Yang, C. P. & Nori, F. Arbitrary control of coherent dynamics for distant qubits in a quantum network. *Phys. Rev. A* **82**, 042327 (2010).
- [23] Osnaghi, S. et al. Coherent Control of an Atomic Colli-

- sion in a Cavity. *Phys. Rev. Lett.* **87**, 037902 (2001).
- [24] Fedorov, A., Steffen, L., Baur, M. & Wallraff, A. Implementation of a Toffoli gate with superconducting circuits. *Nature* (London) **481**, 170-172 (2012).
- [25] Reed, M. D. et al. Realization of three-qubit quantum error correction with superconducting circuits. *Nature* (London) **482**, 382-385 (2012).
- [26] Zhong, Y. P. et al. Emulating anyonic fractional statistical behavior in a superconducting quantum circuit. *Phys. Rev. Lett.* **117**, 110501 (2016).
- [27] Song, C. et al. 10-qubit entanglement and parallel logic operations with a superconducting circuit. *Phys. Rev. Lett.* **119**, 180511 (2017).
- [28] Xu. K. et al. Emulating many-body localization with a superconducting quantum processor. *Phys. Rev. Lett.* **120**, 050507 (2018).
- [29] Ning, W. et al. Deterministic entanglement swapping in a superconducting circuit. *Phys. Rev. Lett.* **123**, 060502 (2019).
- [30] Song, C. et al. Generation of multicomponent atomic Schrödinger cat states of up to 20 qubits. *Science* **365**, 574-577 (2019).
- [31] Wootters, W. K. Entanglement of formation of an arbitrary state of two qubits. *Phys. Rev. Lett.* **80**, 2245-2248 (1998).
- [32] Buzek, V., Braunstein, S. L., Hillery, M. & Bruß, D. Quantum copying: a network. *Phys. Rev. A* **56**, 3446-3452 (1997).

Supplementary Material for: Experimental demonstration of entanglement-enabled universal quantum cloning in a circuit

Zhen-Biao Yang¹, Pei-Rong Han¹, Xin-Jie Huang¹, Wen Ning¹, Hekang Li², Kai Xu^{2,3,*}, Dongning Zheng^{2,3}, Heng Fan^{2,3,†} and Shi-Biao Zheng^{1‡}

1. Fujian Key Laboratory of Quantum Information and Quantum Optics,
College of Physics and Information Engineering,
Fuzhou University, Fuzhou, Fujian 350108, China

2. Institute of Physics and Beijing National Laboratory for Condensed Matter Physics,
Chinese Academy of Sciences, Beijing 100190, China and

3. CAS Center for Excellence in Topological Quantum Computation,
University of Chinese Academy of Sciences, Beijing 100190, China

SUPPLEMENTARY NOTE 1: Quantum entanglement in the output state of an ideal UQCM

When one of the copying qubits is traced out, the joint density matrix for the other copy qubit and the original qubit at the output of the UQCM, in the basis $\{|0_1 0_k\rangle, |0_1 1_k\rangle, |1_1 0_k\rangle, |1_1 1_k\rangle\}$ ($k = 2$ or 3), is given by

$$\rho = \begin{pmatrix} \frac{1}{6}|\alpha|^2 & \frac{1}{3}\alpha\beta^* & \frac{1}{6}\alpha\beta^* & 0 \\ \frac{1}{3}\alpha^*\beta & \frac{1}{6}|\alpha|^2 + \frac{2}{3}|\beta|^2 & \frac{1}{3} & \frac{1}{6}\alpha\beta^* \\ \frac{1}{6}\alpha^*\beta & \frac{1}{3} & \frac{2}{3}|\alpha|^2 + \frac{1}{6}|\beta|^2 & \frac{1}{3}\alpha\beta^* \\ 0 & \frac{1}{6}\alpha^*\beta & \frac{1}{3}\alpha^*\beta & \frac{1}{6}|\beta|^2 \end{pmatrix}. \quad (1)$$

The corresponding $\tilde{\rho}$ matrix, defined as $\tilde{\rho} = \rho(\sigma_y \otimes \sigma_y)\rho^*(\sigma_y \otimes \sigma_y)$, is

$$\tilde{\rho} = \begin{pmatrix} -\frac{1}{9}|\alpha\beta|^2 & \frac{1}{9}\alpha\beta^*(2|\alpha|^2 + |\beta|^2) & \frac{1}{9}\alpha\beta^*(|\alpha|^2 + 2|\beta|^2) & \frac{-1}{9}(\alpha\beta^*)^2 \\ -\frac{1}{9}\alpha^*\beta(|\alpha|^2 + 2|\beta|^2) & \frac{2}{9}|\alpha|^4 + \frac{5}{9}|\alpha\beta|^2 + \frac{2}{9}|\beta|^4 & \frac{1}{9}|\alpha|^4 + \frac{4}{9}|\alpha\beta|^2 + \frac{4}{9}|\beta|^4 & \frac{-1}{9}\alpha\beta^*(|\alpha|^2 + 2|\beta|^2) \\ \frac{-1}{9}\alpha^*\beta(2|\alpha|^2 + |\beta|^2) & \frac{4}{9}|\alpha|^4 + \frac{4}{9}|\alpha\beta|^2 + \frac{1}{9}|\beta|^4 & \frac{2}{9}|\alpha|^4 + \frac{5}{9}|\alpha\beta|^2 + \frac{2}{9}|\beta|^4 & \frac{-1}{9}\alpha\beta^*(2|\alpha|^2 + |\beta|^2) \\ \frac{-1}{9}(\alpha^*\beta)^2 & \frac{1}{9}\alpha^*\beta(2|\alpha|^2 + |\beta|^2) & \frac{1}{9}\alpha^*\beta(|\alpha|^2 + 2|\beta|^2) & \frac{-1}{9}|\alpha\beta|^2 \end{pmatrix}. \quad (2)$$

The four eigenvalues of $\tilde{\rho}$ in the decreasing order are $\lambda_1 = 4/9$ and $\lambda_2 = \lambda_3 = \lambda_4 = 0$, respectively. The corresponding concurrence [1], defined as $C = \max\{\sqrt{\lambda_1} - \sqrt{\lambda_2} - \sqrt{\lambda_3} - \sqrt{\lambda_4}, 0\}$, is $2/3$, which is independent of the input state.

After tracing over the original qubit, the joint density matrix of Q_2 and Q_3 at the output of the UQCM, in the basis $\{|0_2 0_3\rangle, |0_2 1_3\rangle, |1_2 0_3\rangle, |1_2 1_3\rangle\}$, reads as

$$\rho = \begin{pmatrix} \frac{2}{3}|\alpha|^2 & \frac{1}{3}\alpha\beta^* & \frac{1}{3}\alpha\beta^* & 0 \\ \frac{1}{3}\alpha^*\beta & \frac{1}{6} & \frac{1}{6} & \frac{1}{3}\alpha\beta^* \\ \frac{1}{3}\alpha^*\beta & \frac{1}{6} & \frac{1}{6} & \frac{1}{3}\alpha\beta^* \\ 0 & \frac{1}{3}\alpha^*\beta & \frac{1}{3}\alpha^*\beta & \frac{2}{3}|\beta|^2 \end{pmatrix}. \quad (3)$$

The matrix $\tilde{\rho}$ is

$$\tilde{\rho} = \begin{pmatrix} \frac{2}{9} |\alpha\beta|^2 & \frac{1}{9} \alpha\beta^* (|\beta|^2 - |\alpha|^2) & \frac{1}{9} \alpha\beta^* (|\beta|^2 - |\alpha|^2) & \frac{-2}{9} (\alpha\beta^*)^2 \\ \frac{1}{9} \alpha^* \beta (|\beta|^2 - |\alpha|^2) & \frac{1}{18} - \frac{2}{9} |\alpha\beta|^2 & \frac{1}{18} - \frac{2}{9} |\alpha\beta|^2 & \frac{1}{9} \alpha\beta^* (|\alpha|^2 - |\beta|^2) \\ \frac{1}{9} \alpha^* \beta (|\beta|^2 - |\alpha|^2) & \frac{1}{18} - \frac{2}{9} |\alpha\beta|^2 & \frac{1}{18} - \frac{2}{9} |\alpha\beta|^2 & \frac{1}{9} \alpha\beta^* (|\alpha|^2 - |\beta|^2) \\ \frac{-2}{9} (\alpha^* \beta)^2 & \frac{1}{9} \alpha^* \beta (|\alpha|^2 - |\beta|^2) & \frac{1}{9} \alpha^* \beta (|\alpha|^2 - |\beta|^2) & \frac{2}{9} |\alpha\beta|^2 \end{pmatrix}, \quad (4)$$

the four eigenvalues of which in the decreasing order are $\lambda_1 = 1/9$ and $\lambda_2 = \lambda_3 = \lambda_4 = 0$, respectively, corresponding to a concurrence of $1/3$, which is also input-state-independent.

SUPPLEMENTARY NOTE 2: Effects of

asymmetric direct couplings

With direct asymmetric couplings between the qubits being considered, the system finally evolves to the state

$$\begin{aligned} & \alpha \left[\sqrt{\frac{2}{3}} k_1 e^{i\theta} |1_1 0_2 0_3\rangle + \sqrt{\frac{1}{6}} |0_1\rangle (k_2 e^{i\phi_2} |1_2 0_3\rangle + k_3 e^{i\phi_3} |0_2 1_3\rangle) \right] \\ & + \beta \left[\sqrt{\frac{2}{3}} k_4 e^{i\phi_4} |0_1 1_2 1_3\rangle + \sqrt{\frac{1}{6}} e^{i\theta} |1_1\rangle (k_5 e^{i\phi_5} |1_2 0_3\rangle + k_6 e^{i\phi_6} |0_2 1_3\rangle) \right]. \end{aligned} \quad (5)$$

The reduced density operator for Q_2 and Q_3 after tracing out Q_1 is given by

$$|\psi_1\rangle \langle \psi_1| + |\psi_2\rangle \langle \psi_2|, \quad (6)$$

where

$$\begin{aligned} |\psi_1\rangle &= \sqrt{\frac{2}{3}} \alpha k_1 e^{i\theta} |0_2 0_3\rangle \\ &+ \sqrt{\frac{1}{6}} \beta e^{i\theta} (k_5 e^{i\phi_5} |1_2 0_3\rangle + k_6 e^{i\phi_6} |0_2 1_3\rangle), \end{aligned} \quad (7)$$

and

$$|\psi_2\rangle = \sqrt{\frac{1}{6}} \alpha (k_2 e^{i\phi_2} |1_2 0_3\rangle + k_3 e^{i\phi_3} |0_2 1_3\rangle) + \sqrt{\frac{2}{3}} \beta k_4 e^{i\phi_4} |1_2 1_3\rangle. \quad (8)$$

The concurrence between Q_2 and Q_3 is given by

$$\mathcal{E}_{2,3} = \frac{1}{3} \left| |\alpha|^2 k_2 k_3 e^{i(\phi_2 - \phi_3)} + |\beta|^2 k_5 k_6 e^{i(\phi_5 - \phi_6)} \right|. \quad (9)$$

For $k_j \approx 1$ with $j = 1$ to 5 , we have

$$\mathcal{E}_{2,3} \approx \frac{1}{3} \left| |\alpha|^2 e^{i(\phi_2 - \phi_3)} + |\beta|^2 e^{i(\phi_5 - \phi_6)} \right|. \quad (10)$$

When $\beta = 0$ or 1 , we have $\mathcal{E}_{2,3} \approx \frac{1}{3}$. For $|\beta| = 1/\sqrt{2}$, $\mathcal{E}_{2,3} \approx \frac{1}{3} \cos \delta$, where $\delta = (\phi_2 + \phi_6 - \phi_3 - \phi_5)/2$. This implies that the output Q_2 - Q_3 entanglement for the input superposition state may be much smaller than that for the input $|0\rangle$ - or $|1\rangle$ -state.

When Q_1 and Q_2 are traced out, the reduced density matrix for Q_3 is given by

	$\omega_j/2\pi$ (GHz)	$g_j/2\pi$ (MHz)	$\lambda_{j,j+1}/2\pi$ (MHz)	$T_{1,j}$ (μ s)	$T_{2,j}^*$ (μ s)	$T_{2,j}^{\text{SE}}$ (μ s)	$1/\kappa_j^r$ (ns)	$F_{0,j}$	$F_{1,j}$
Q_1	5.367	20.0	0.069	24.0(15.4)	2.2(2.4)	6.5(6.9)	315	0.984	0.925
Q_2	5.223	20.8	0.553	25.8(28.5)	0.7(0.9)	6.2(7.1)	219	0.988	0.939
Q_3	5.311	19.9	-0.066	22.7(14.4)	2.6(2.9)	8.0(8.9)	203	0.986	0.921

Supplementary Table 1: Qubits characteristics. $\omega_j/2\pi$ is the idle frequency of Q_j where single-qubit rotations and qubit state tomography are performed. g_j is the coupling strength between Q_j and the bus resonator. $\lambda_{j,j+1}$ is the magnitude of crosstalk qubit-qubit coupling between Q_j and Q_{j+1} beyond that induced by the resonator. $T_{1,j}$, $T_{2,j}^*$, and $T_{2,j}^{\text{SE}}$ are the energy relaxation time, the Ramsey dephasing time (Gaussian decay), and the dephasing time (Gaussian decay) with spin-echo, respectively, all of them (those in parentheses) are measured at the idle (working) point of Q_j . κ_j^r represents the leakage rate of Q_j 's readout resonator R_j . $F_{0,j}$ ($F_{1,j}$) is the probability of correctly detecting Q_j in $|0\rangle$ ($|1\rangle$) when it is prepared in $|0\rangle$ ($|1\rangle$).

$$\rho_3 = \begin{pmatrix} \frac{2}{3}|\alpha k_1|^2 + \frac{1}{6}|\alpha k_2|^2 + \frac{1}{6}|\beta k_5|^2 & \frac{1}{3}\alpha\beta^* k_1 k_6 e^{-i\phi_6} + \frac{1}{3}\alpha\beta^* k_2 k_4 e^{i(\phi_2 - \phi_4)} \\ \frac{1}{3}\alpha^* \beta k_1 k_6 e^{i\phi_6} + \frac{1}{3}\alpha^* \beta k_2 k_4 e^{-i(\phi_2 - \phi_4)} & \frac{1}{6}|\alpha k_3|^2 + \frac{1}{6}|\beta k_6|^2 + \frac{2}{3}|\beta k_4|^2 \end{pmatrix}. \quad (11)$$

For $k_j \approx 1$, we have

$$\rho_3 \approx \begin{pmatrix} \frac{5}{6}|\alpha|^2 + \frac{1}{6}|\beta|^2 & \frac{1}{3}\alpha\beta^* [e^{-i\phi_6} + e^{i(\phi_2 - \phi_4)}] \\ \frac{1}{3}\alpha^* \beta [e^{i\phi_6} + e^{-i(\phi_2 - \phi_4)}] & \frac{1}{6}|\alpha|^2 + \frac{5}{6}|\beta|^2 \end{pmatrix}. \quad (12)$$

The corresponding fidelity is

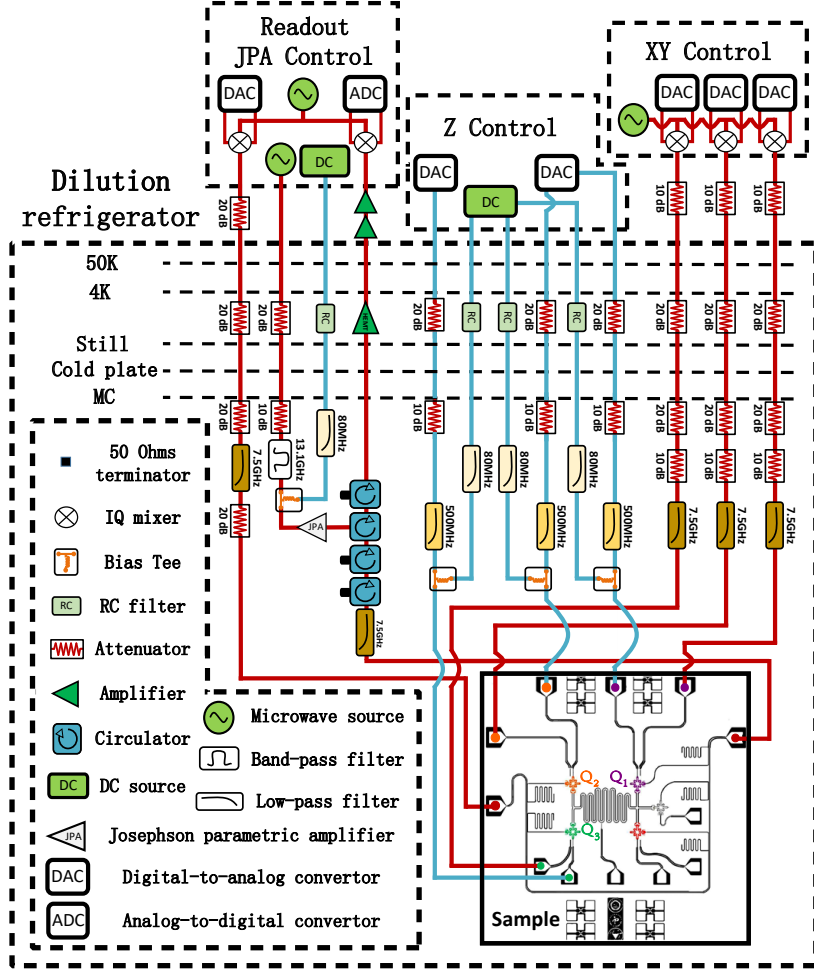
$$F \approx \begin{pmatrix} \alpha^* & \beta^* \end{pmatrix} \begin{pmatrix} \frac{5}{6}|\alpha|^2 + \frac{1}{6}|\beta|^2 & \frac{1}{3}\alpha\beta^* [e^{-i\phi_6} + e^{i(\phi_2 - \phi_4)}] \\ \frac{1}{3}\alpha^* \beta [e^{i\phi_6} + e^{-i(\phi_2 - \phi_4)}] & \frac{1}{6}|\alpha|^2 + \frac{5}{6}|\beta|^2 \end{pmatrix} \begin{pmatrix} \alpha \\ \beta \end{pmatrix} \quad (13)$$

$$= |\alpha|^2 \left(\frac{5}{6}|\alpha|^2 + \frac{1}{6}|\beta|^2 \right) + \frac{2}{3}|\alpha\beta|^2 [\cos \phi_6 + \cos(\phi_2 - \phi_4)] + |\beta|^2 \left(\frac{1}{6}|\alpha|^2 + \frac{5}{6}|\beta|^2 \right).$$

When $\beta = 0$ or 1 , we have $F \approx \frac{5}{6}$. For $|\beta| = 1/\sqrt{2}$, $F \approx \frac{1}{2} + \frac{1}{6}[\cos \phi_6 + \cos(\phi_2 - \phi_4)]$. When $\phi_6 \approx 2m\pi$ and $\phi_2 - \phi_4 \approx 2n\pi$, with m and n being integers, the fidelities for the input superposition states are almost the same as those for the input $|0\rangle$ - or $|1\rangle$ -state.

SUPPLEMENTARY NOTE 3: Device sketch, system parameters and experimental setup

The UQCM is demonstrated in a superconducting circuit consisting of five frequency-tunable Xmon qubits, labeled from Q_1 to Q_5 , coupled to a resonator with a fixed frequency of $\omega_r/2\pi = 5.588$ GHz [3, 4], as sketched in Supplementary Figure 1. Q_4 and Q_5 (not marked here), not used in the experiment, stay far off-resonant from the other three qubits and the resonator throughout the copying process. The parameters are detailed in



Supplementary Figure 1: Sketch of the device and experimental setup. At the right-bottom side: the device (sample) consists of five frequency-tunable superconducting Xmon qubits, denoted by Q_j with $j = 1$ to 5, coupled to a bus resonator, labeled as R . Q_1 acts as the input qubit, whose state is to be copied onto Q_2 and Q_3 . Q_4 and Q_5 are unused and not marked here. All the electronics and wiring is shown, from right to left, for the qubit XY control, the qubit Z control, the qubit readout and JPA control, respectively. Each qubit XY control is produced by the mixing of the signals of two independent DAC channels I/Q and a microwave source, and used for the fast qubit flipping. Each qubit Z control has two channels of signals: the Z pulse control directly produced by a DAC channel for the fast frequency tuning of the qubit and the DC control provided by a DC source for resetting its operating point. The qubit readout signal is provided also by the sideband mixing of the signals of two independent DAC channels I/Q and a microwave source, outputting a three-tone microwave pulse that targets the readout resonators of all the qubits. The output signal is amplified sequentially by JPA, HEMT and room temperature amplifiers, before being captured and demodulated by the ADC. The JPA control is provided by the pumping of an independent microwave signal with its amplification band being tunable with a DC bias applied to it. Each control line is fed with well-designed attenuators and filters to prevent the unwanted noise from disturbing the operation of the device.

Supplementary Table 1. The qubit-resonator coupling strength g_j is measured and estimated through the vacuum Rabi oscillations. The qubits' energy decaying time T_1 , the Ramsey dephasing time $T_{2,j}^*$, and the dephasing time with spin-echo $T_{2,j}^{SE}$ are respectively measured at

qubits' idle frequencies ω_j ; while the values in parentheses are those measured at the qubits' working frequency $\omega_w/2\pi = 5.44$ GHz where the resonator-induced qubit-qubit couplings are realized and used for the Bell-state generation and the cloning operation. The leakage rate

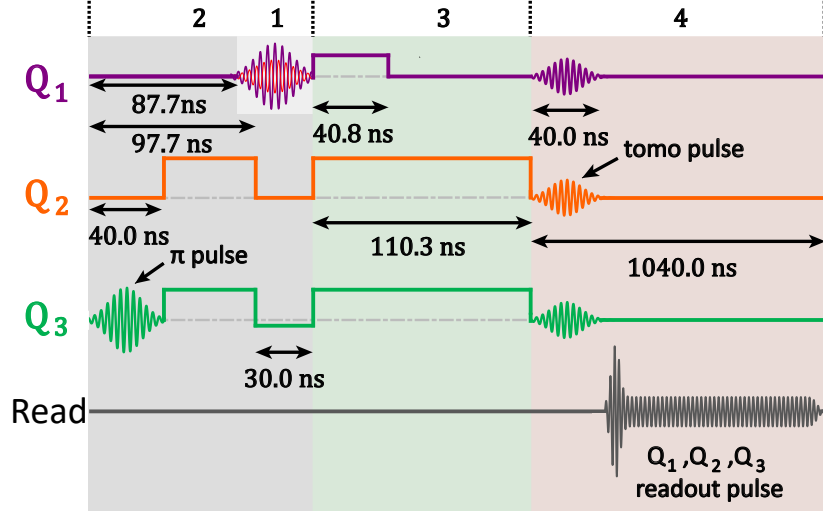
κ_j^r of Q_j 's readout resonator R_j is obtained through measuring the frequency shift of Q_j induced by photons accumulated in its readout resonator [4, 5]. $F_{0,j}$ ($F_{1,j}$) is the probability of detecting Q_j in $|0\rangle$ ($|1\rangle$) when it is prepared in $|0\rangle$ ($|1\rangle$). More details about the device performance are described in the Supplementary Materials of Refs. [3, 4].

The whole electronics and wiring for the device control is separated into two parts: one at room temperature and the other in the dilution refrigerator, as shown in Supplementary Figure 1. Each qubit XY control is implemented through the mixing of the low-frequency signals produced by 2 Digital-to-analog convertor (DAC) channels (I/Q) and a Microwave source (MS) whose carry frequency is 5.52 GHz; it realizes the fast qubit flipping at the nanosecond scale. Each qubit's frequency control is implemented by the signals from two ways that are combined from a bias tee, one is directly produced by a DAC channel for the fast tuning of the qubit's frequency, while the other is sent by a Direct-current (DC) channel to reset the qubit's frequency to specific operating point. The qubit readout control is achieved also by the sideband mixing of the signals of two independent DAC channels I/Q and a MS with the frequency of 6.67 GHz, thus it outputs a readout pulse with 3 tones that targets 3 qubits' readout resonators. The output from the sample is amplified sequentially by the impedance-transformed Josephson parametric amplifier (JPA), high electron mobility transistor (HEMT) and room temperature amplifiers before being captured and demodulated by ADC. 4 cryogenic circulators with low insertion loss are placed between JPA and the device to allow the unidirectional-transmission of microwave signal which impedes the reflections and noise from the input entering into the device. The JPA is pumped by a MS with the frequency of 13.494 GHz, about twice the signal frequency through

the pumping line, where the signal is filtered by a 13.1 GHz band-pass filter; the amplification band of the JPA is tunable with a DC bias applied to it. To reduce kinds of unwanted noises feeding into the signal lines, each signal from (to) DAC and Analog-to-digital convertor (ADC) is filtered with a 7.5 GHz low-pass filter, each qubit Z pulse from DAC is filtered with a 500 MHz low-pass filter, and each DC signal is filtered with a 80 MHz low-pass filter at Mixing-Chamber (MC) stage and with a RC filter at 4K state. Moreover, some attenuators are also added to the signal lines at different temperature stages to further reduce the noises influencing the operation of the device.

SUPPLEMENTARY NOTE 4: Experimental pulse sequences

The pulse sequence for UQCM is shown in Supplementary Figure 2, which is divided into 3 stages in time series. The first stage involves 2 steps for the implementation: the preparation of the state to be cloned for Q_1 and the preparation of the entangled state for the two copy qubits Q_2 and Q_3 . The experiment begins with a π rotation X_π applied on Q_3 , realized by a microwave pulse with a duration of 40 ns at its idle frequency. Then Q_2 and Q_3 are biased with rectangular pulses from their respective idle frequencies (see Supplementary Table 1) to the working frequency $\omega_w/2\pi = 5.44$ GHz, which is red-detuned from the resonator frequency by an amount of $\Delta = 2\pi \times 148$ MHz. Thus it implements a $\sqrt{i\text{SWAP}}$ gate and steers Q_2 - Q_3 to the entangled state $|\psi_{2,3}\rangle = [e^{i(\pi/2+\theta_d)} |1_20_3\rangle + |0_21_3\rangle] / \sqrt{2}$, with θ_d being the dynamical phase accumulated during the frequency tuning process. A compensated Z-pulse is applied to Q_3 for 30 ns to eliminate the factor $e^{i(\pi/2+\theta_d)}$ of such an entangled state $|\psi_{2,3}\rangle$. Meanwhile, Q_1 is prepared to the initial state to be cloned by microwave pulses sent through its XY control line. The second stage launches by biasing each of the three qubits with



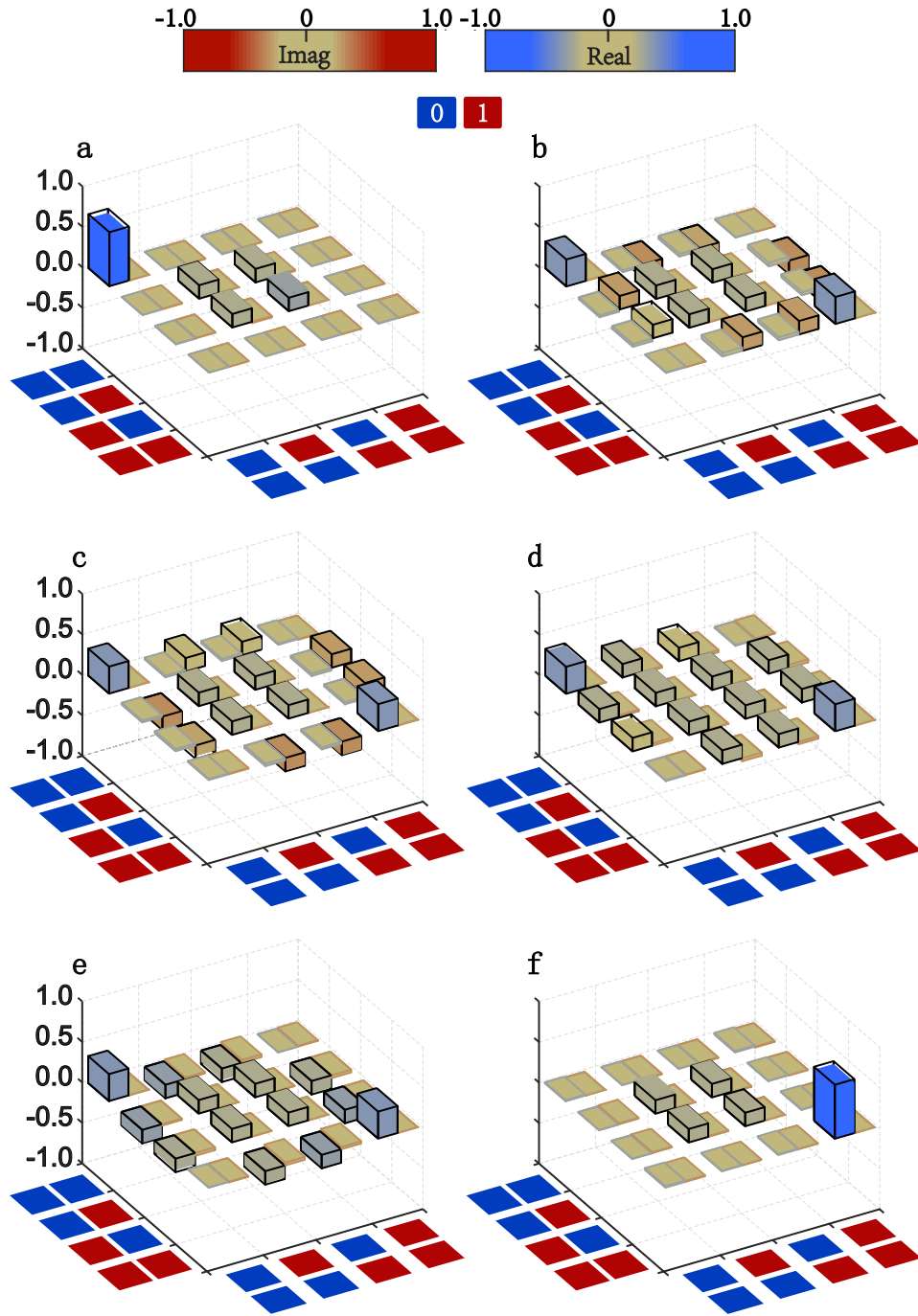
Supplementary Figure 2: Experimental pulse sequence. The sequence is divided into 3 stages which involves 4 steps: 1. the preparation of the state to be cloned for Q_1 ; 2. the preparation of the entangled state for Q_2 and Q_3 ; 3. resonator-induced couplings $C_{1,2,3}$ and $C_{2,3}$; and 4. quantum state tomography. In the first stage, a microwave π -pulse with a duration of 40 ns is first applied on Q_3 to excite it to $|1_3\rangle$, then a rectangular pulse with a length of 57.7 ns is applied on the qubit pair Q_2 - Q_3 to tune them on resonance, realizing the $\sqrt{i\text{SWAP}}$ gate which generates the entangled state $[e^{i(\pi/2+\theta_d)} |1_20_3\rangle + |0_21_3\rangle] / \sqrt{2}$. A compensated rectangular pulse of a length of 30 ns is then applied on Q_3 to cancel the phase factor i and the dynamical phase θ_d accumulated during the frequency tuning process. The step 1 for the preparation of the input state to be cloned for Q_1 begins in the last 40 ns of the step 2, through a microwave pulse that terminates synchronously with the phase compensated pulse. In step 3, the resonator-induced coupling $C_{1,2,3}$ is started with a rectangular pulse applied on each qubit: Q_1 , Q_2 , and Q_3 , tuning them on resonance for about 40.8 ns; this is successively transformed to the coupling $C_{2,3}$ as the rectangular pulse on Q_1 is withdrawn at the moment thus remaining only Q_2 and Q_3 virtually coupling with the resonator, the duration is about 69.5 ns. Note that a single-qubit z-axis rotation is then numerically applied on each qubit to cancel the extra phase accumulated due to the qubits' frequency shift during the process. The sequence of step 4 involves a tomographic pulse of a duration 40 ns and a readout pulse of a duration of 1 μs on each qubit. Thus the density matrix for each qubit and the joint density matrices for any two qubits can be reconstructed.

a rectangular pulse to the working frequency ω_w , realizes the resonator-induced three-qubit coupling $C_{1,2,3}$ for the preparation of the three-body state in Eq. (4) of the main text and the resonator-induced two-qubit coupling $C_{2,3}$ for the neutralization of the phase factor $e^{-i\pi/3}$ in such a three-body state. The processes $C_{1,2,3}$ and $C_{2,3}$ last for 40.8 ns and 69.5 ns, respectively. In the third stage, the qubit output state tomography is performed, where three kinds of tomographic pulses (I , $X/2$, $Y/2$) for each qubit are iterated for different experimental run. With this pulse sequence, the density matrices for each of the copying qubits Q_2

and Q_3 associated with the different input states $\{|0_1\rangle, (|0_1\rangle + i|1_1\rangle) / \sqrt{2}, (|0_1\rangle - i|1_1\rangle) / \sqrt{2}, (|0_1\rangle + |1_1\rangle) / \sqrt{2}, (|0_1\rangle - |1_1\rangle) / \sqrt{2}, |1_1\rangle\}$ are reconstructed and displayed in Fig. 2a-f of the main text, respectively. While the joint Q_1 - Q_2 and Q_1 - Q_3 output density matrices associated with the six input states are reconstructed and displaced in Fig. 4a-f of the main text, respectively.

SUPPLEMENTARY NOTE 5: Q_2 - Q_3 joint state tomography

To characterize the quantum entanglement between the two copy qubits after the cloning operation, we perform joint output state tomography for Q_2 and Q_3 .



Supplementary Figure 3: Q_2 - Q_3 joint output density matrices for the six input states: **a** $|0_1\rangle$; **b** $(|0_1\rangle + i|1_1\rangle)/\sqrt{2}$; **c** $(|0_1\rangle - i|1_1\rangle)/\sqrt{2}$; **d** $(|0_1\rangle + |1_1\rangle)/\sqrt{2}$; **e** $(|0_1\rangle - |1_1\rangle)/\sqrt{2}$; **f** $|1_1\rangle$. Each matrix element is characterized by two color bars, one for the real part and the other for the imaginary part. The black wire frames denote the corresponding matrix elements of the ideal output states.

The Q_2 - Q_3 joint output density matrices for the six input states $|0_1\rangle$, $(|0_1\rangle + i|1_1\rangle)/\sqrt{2}$, $(|0_1\rangle - i|1_1\rangle)/\sqrt{2}$, $(|0_1\rangle + |1_1\rangle)/\sqrt{2}$, $(|0_1\rangle - |1_1\rangle)/\sqrt{2}$, $|1_1\rangle$ are shown in

Supplementary Figure 3a-f, respectively. The measured matrix elements are denoted by two color bars, one for the real part and the other for the imaginary part, which

are in well agreement with the corresponding results for a perfect UQCM (black wire frames). Note that for clarity, before the state tomography, a single-qubit z-axis rotation with a specific radian angle (Q1: -0.390; Q2: 0.145; Q3: -0.331.) is numerically applied to cancel the extra phase accumulated due to the qubits' frequency shift, which does not change the entanglement.

SUPPLEMENTARY NOTE 6: The calibration for the measurement

In our experiment, the measured probabilities for reconstructing the system states are calibrated on the basis of the qubits' $|0\rangle$ - and $|1\rangle$ -state measurement fidelities, which are shown in Supplementary Table 1. The calibrated matrix for each qubit is thus constructed to be [3, 4]

$$\hat{F}_j^c = \begin{pmatrix} F_{0,j} & 1 - F_{1,j} \\ 1 - F_{0,j} & F_{1,j} \end{pmatrix}. \quad (14)$$

The system's state density matrix ($\hat{\rho}_N^c$) is reconstructed by correcting the measured probabilities ($\hat{\rho}_N$) by multiplying the matrix inversion as

$$\hat{\rho}_N^c = \hat{F}^{-1} \cdot \hat{\rho}_N, \quad (15)$$

with \hat{F} defined as the tensor product of each qubit's \hat{F}_j^c : $\hat{F} = (\hat{F}_j^c)^{\otimes j}$.

SUPPLEMENTARY NOTE 7: The state and process tomography

In our experiment, states produced at specific stages are characterized and reconstructed by the technique of quantum state tomography (QST). Take a single qubit state, pure or mixed, as an instance, its density operator in the basis $\{|0\rangle, |1\rangle\}$ can be described by

$$\hat{\rho} = \rho_{0,0}|0\rangle\langle 0| + \rho_{0,1}|0\rangle\langle 1| + \rho_{1,0}|1\rangle\langle 0| + \rho_{1,1}|1\rangle\langle 1|. \quad (16)$$

Intuitively, such a state can be visually described as a point lying in or on the Bloch sphere. It's then naturally

to introduce the Bloch vector (connecting the origin of the coordinate to such a point)

$$\vec{r} = \langle \hat{X} \rangle \vec{e}_X + \langle \hat{Y} \rangle \vec{e}_Y + \langle \hat{Z} \rangle \vec{e}_Z, \quad (17)$$

with

$$\begin{aligned} \langle \hat{X} \rangle &= \text{tr}(\hat{\rho} \hat{X}) = \rho_{0,1} + \rho_{1,0}, \\ \langle \hat{Y} \rangle &= \text{tr}(\hat{\rho} \hat{Y}) = i(\rho_{0,1} - \rho_{1,0}), \\ \langle \hat{Z} \rangle &= \text{tr}(\hat{\rho} \hat{Z}) = \rho_{0,0} - \rho_{1,1}. \end{aligned} \quad (18)$$

To locate such a point means to define the state because of $\hat{\rho} = \sum_{\hat{A}=\hat{X},\hat{Y},\hat{Z},I} \langle \hat{A}/2 \rangle \hat{A}$, which requires the three coordinate components, i.e., measured values $\langle \hat{X} \rangle$, $\langle \hat{Y} \rangle$, and $\langle \hat{Z} \rangle$ along the corresponding axes. For the two-level system, a typical measurement reveals the probability P_0 or P_1 for it be in state $|0\rangle$ or $|1\rangle$, that directly translates to the component along the Z-axis giving Z-coordinate: $\langle \hat{Z} \rangle = P_0 - P_1$, i.e., the diagonal elements in Eq. (16). To get the X-coordinate of the state, we rotate about Y by $-\pi/2$ thus bring the X axis to the original position of the Z axis before measurement; while to get the Y-coordinate, we rotate about X by $\pi/2$ before measurement. The last two measurements after the rotations give the non-diagonal elements of Eq. (16). Therefore these three measurements allow the quantum state $\hat{\rho}$ of Eq. (16) to be completely reconstructed. Suppose a system of N qubits, we perform 3^N possible combinations of rotations on the qubits: $U^j \in \{X/2, Y/2, I\}^{\otimes N}$, and measure the system to count 2^N probabilities of $\{P_{00\dots 0}, P_{00\dots 1}, \dots, P_{11\dots 1}\}$:

$$\begin{aligned} P_k^j &= \rho_{kk}^j = \langle k|U^j \rho (U^j)^\dagger|k\rangle, \\ k &= 1, 2, \dots, 2^N, \quad j = 1, 2, \dots, 3^N. \end{aligned} \quad (19)$$

Each combination of rotations needs a pulse sequence, in which we append a tomographic operation for each qubit after producing the state, and then measure the binary outcomes of the N qubits. We repeat the same

sequence thousands of times to count all the probabilities. Taking into account the condition of normalization, these measurements produce $3^N(2^N - 1)$ numbers to determine the N qubits' density matrix $\hat{\rho}_N$, that possesses $4^N - 1$ degrees of freedom. Owing to the condition of $3^N(2^N - 1) \geq 4^N - 1$, the measurement outcomes give more than enough information to determine $\hat{\rho}_N$. By introducing the vector form $\tilde{P}_O = P_k^j$ and $\tilde{\rho}_N = \hat{\rho}_N$, we simplify Eq. (19) as

$$\tilde{P}_O = \tilde{U}\tilde{\rho}_N, \quad (20)$$

with \tilde{U} being the tensor object formed by the combination of U^j and $(U^j)^+$. As the problem in the form of Eq. (20) is overconstrained, for our implementation we solved it by turning to a least-squares optimization as to find the optimal solution. Due to the inevitable noises involved in the measured quantities, conversely it is helpful to use the overdetermined equations to guarantee the availability of the outcomes. Nevertheless, the solved $\hat{\rho}_N$ through such a method does not necessarily ensure that it is positive, Hermitian, and semi-definite with unit trace. It is still needed another optimization, that is, $\min(\|\hat{\rho}_N - \hat{\rho}'_N\|)$, to get the required $\hat{\rho}'_N$ that satisfies the three conditions imposed. Then the fidelity of the qubit state can be obtained by the calculation

$$F = \text{tr}(\hat{\rho}'_N * \hat{\rho}_{id}), \quad (21)$$

where $\hat{\rho}_{id}$ is the ideal density matrix. Note that the reconstructed density matrices for the fidelity calculation are calibrated according to the qubits' $|0\rangle$ - and $|1\rangle$ -state measurement fidelities, as shown in Supplementary note 5.

The quantum process tomography (QPT) characterizes certain evolution processes for quantum operations. These quantum operations can be described by the operator-sum representation:

$$\mathcal{M}(\hat{\rho}) = \sum_i \hat{B}_i \hat{\rho} \hat{B}_i^+. \quad (22)$$

Such a linear map \mathcal{M} completely describes the dynamics of the system, whose states could change due to not only any unitary operation performed by kinds of quantum gates, but also projection or decoherence effect that are not unitary. The operators \hat{B}_i act on the system alone, and satisfy the completeness relation $\sum_i \hat{B}_i^+ \hat{B}_i = I$ to guarantee $\text{Tr}[\mathcal{M}(\rho)] = 1$. The key is to determine the operators \hat{B}_i in experiment for a specific quantum process. To do so, it's required to relate the \hat{B}_i to measurable values and expand them with a linear combination of a set of operators \tilde{B}_i :

$$\hat{B}_i = \sum_h b_{ih} \tilde{B}_h, \quad (23)$$

while not changing the description of \mathcal{M} , provided the \tilde{B}_h form a set of complete operation bases acting on the state space, and b_{ih} are certain complex numbers. The mapping in Eq. (22) is thus rewritten as

$$\mathcal{M}(\rho) = \sum_{hv} \tilde{B}_h \hat{\rho} \tilde{B}_v^+ \chi_{hv}, \quad (24)$$

where $\chi_{hv} = \sum_i b_{ih} b_{iv}^*$. Obviously, the χ_{hv} are determined by the \tilde{B}_h , and completely describe the whole mapping process provided the \tilde{B}_h are fixed.

We now show how to determine χ_{hv} experimentally. Consider a N-qubit system, whose initial state can be expressed as a $2^N \times 2^N$ matrix. The matrix can be written as the unique linear combination of $\hat{\rho}_j$, with $\hat{\rho}_j$ being the linearly independent basis element within the matrix. It's convenient to choose the basis operator $\hat{\rho}_{hv} \equiv |h\rangle\langle v|$, and by preparing a set of preset input states, commonly, such as $|j\rangle \in \{|h\rangle, |v\rangle, (|h\rangle + |v\rangle)/\sqrt{2}, (|h\rangle + i|v\rangle)/\sqrt{2}\}$, after the process transformation due to the system's changing, it is then natural to produce the output $\mathcal{M}(\hat{\rho}_j)$, which is formed by linear combinations of $\mathcal{M}(|j\rangle\langle j|)$, as can be determined by quantum state tomography. Therefore, it is reasonable to express $\mathcal{M}(\hat{\rho}_j)$ as a linear combination

of the basis states:

$$\mathcal{M}(\hat{\rho}_j) = \sum_k \eta_{jk} \hat{\rho}_k, \quad (25)$$

which determines η_{jk} based on the known $\mathcal{M}(\hat{\rho}_j)$.

Going back to Eq. (24), we write within it the relation:

$$\tilde{B}_h \hat{\rho}_j \tilde{B}_v^+ = \sum_k \xi_{jk}^{hv} \hat{\rho}_k, \quad (26)$$

which determines ξ_{jk}^{hv} given the \tilde{B}_h operators and the $\hat{\rho}_j$ operators. Combining Eqs. (24) and (25), we have

$$\sum_k \sum_{hv} \chi_{hv} \xi_{jk}^{hv} \hat{\rho}_k = \sum_k \eta_{jk} \hat{\rho}_k. \quad (27)$$

Eq. (27) immediately gives

$$\sum_{hv} \chi_{hv} \xi_{jk}^{hv} = \eta_{jk} \quad (28)$$

due to that $\hat{\rho}_k$ is linearly independent. The generalized inverse ς of ξ_{jk}^{hv} can be solved with the help of specific software packages for matrix calculation. Thus χ_{jk}^{hv} can then be obtained to be

$$\chi_{hv} = \sum_{jk} \varsigma_{jk}^{hv} \eta_{jk}. \quad (29)$$

- [1] Wootters, W. K. Entanglement of formation of an arbitrary state of two qubits. *Phys. Rev. Lett.* **80**, 2245-2248 (1998).
- [2] James, D. F. V. & Jerke, J. Effective Hamiltonian theory and its applications in quantum information. *Can. J. Phys.* **85**, 625-632 (2007).
- [3] Song, C. et al. Continuous-variable geometric phase and its manipulation for quantum computation in a supercon-

- ducting circuit. *Nat. Commun.* **8**, 1061 (2017).
- [4] Ning, W. et al. Deterministic entanglement swapping in a superconducting circuit. *Phys. Rev. Lett.* **123**, 060502 (2019).
- [5] Sank, D. Fast, accurate state measurement in superconducting qubits. Ph. D. thesis, University of California Santa Barbara, 2014.